Insight into the synergistic effect of 2D/2D layered metal selenides wrapped nickel boride nanoparticles based ternary heterostructure for constructing asymmetric supercapacitors with excellent energy density

Ramaraj Sukanya [a,1], Raj Karthik [b,1], Mahmudul Hasan [b,1], Carmel Breslin [a,*], Jae-Jin Shim [b,*]

[a] Department of Chemistry, Maynooth University, Maynooth, Co. Kildare, Ireland
[b] School of Chemical Engineering, Yeungnam University, Gyeongsan, Gyeongbuk 38541, Republic of Korea

ARTICLE INFO

ABSTRACT

Tuning the structural and electronic properties of layered metal selenides is a highly feasible approach for developing high-performance asymmetric supercapacitors (ASCs). In this work, a ternary heterostructure of yttrium diselenide/molybdenum diselenide ($YSe_2/MoSe_2$) with amorphous nickel boride nanoparticles (Ni_xB NPs) was prepared by a simple hydrothermal method followed by a liquid phase route. Interestingly, this ternary heterostructure consists of multiple layers of $YSe_2/MoSe_2$ nanosheets uniformly wrapped by Ni_xB NPs over the entire surface. The characterization results by X-ray diffraction, Raman, and X-ray photoelectron spectroscopy showed that the strong synergism between $YSe_2/MoSe_2$ and Ni_xB NPs indicates an obvious electron transfer from Ni_xB to the $YSe_2/MoSe_2$ hybrid, which contributes to the enhancement of the electrical conductivity of the electrode. Due to its exclusive heterostructure network, the single $YSe_2/MoSe_2/Ni_xB$ electrode achieved a specific capacitance of 893.3 F/g at 1 A/g and a capacity retention of 128.17% over 5000 cycles. In addition, the asymmetric $YSe_2/MoSe_2/Ni_xB||rGO$ device with a working potential of 1.6 V showed an impressive energy density of 39.5 Wh kg^{-1} with a power density of 800 W kg^{-1} and excellent cycling stability with 85.60% capacity retention after 5000 cycles in aqueous electrolyte. This result of the designed ASC device encourages the development of a new platform for the design of electrode materials based on metal selenides and metal borides.

1. Introduction

Supercapacitors (SCs) are considered promising energy storage devices for addressing energy demand challenges due to their remarkable performance in terms of fast charge/discharge characteristics, high power density, long lifetime, and cost efficiency [1,2]. However, their practical application is limited due to their lower energy density compared to batteries. To solve this problem, the development of a highly active positive electrode material with high energy density is urgently needed to meet the energy demand criteria [3]. As a well-known cathodic material, transition metal selenides have emerged as potential candidates for SCs due to their high electrical conductivity and excellent electrochemical activity [3]. Due to its unique physicochemical properties and special sheet-like structure, 2D layered $MoSe_2$ is one of the most active electrode materials for battery-type SCs [4]. $MoSe_2$ exhibits several remarkable properties, including mixed oxidation states, large surface area, electrochemically active unsaturated edge sites, high theoretical specific capacitance, excellent redox behavior, and high volumetric energy density [5]. On this basis, *Pazhamalai* et al. developed a 2H-$MoSe_2$ nanosheet-based electrode for symmetric SC and achieved a specific cell capacitance of 16.25 F/g with an energy density of 20.31 Wh kg^{-1} in an organic electrolyte medium [6]. Recently, *Rahul* and *Kumar Arora* et al. synthesized few-layer $MoSe_2$ nanosheets and used them as electrodes for SCs, which showed a capacitance of 15 F/g and achieved an efficiency of 95% over 12 repeated cycles. This report concludes that the layered $MoSe_2$ sheets provide good specific capacitance due to the maximum accessible surface area [7]. However, the studies on $MoSe_2$ as a single active electrode material show that agglomeration can easily occur due to Van der Waals forces, which limits the charge transfer rate and leads to a decrease in specific capacitance and a capacitance fading during longer cycles [8,9]. Moreover, the inactive basal planes of layered $MoSe_2$ reduce the

---

* Corresponding authors.
  E-mail addresses: carmel.Breslin@mu.ie (C. Breslin), jjshim@yu.ac.kr (J.-J. Shim).
[1] Authors R. Sukanya, R. Karthik, and M. Hasan contributed equally to this manuscript.
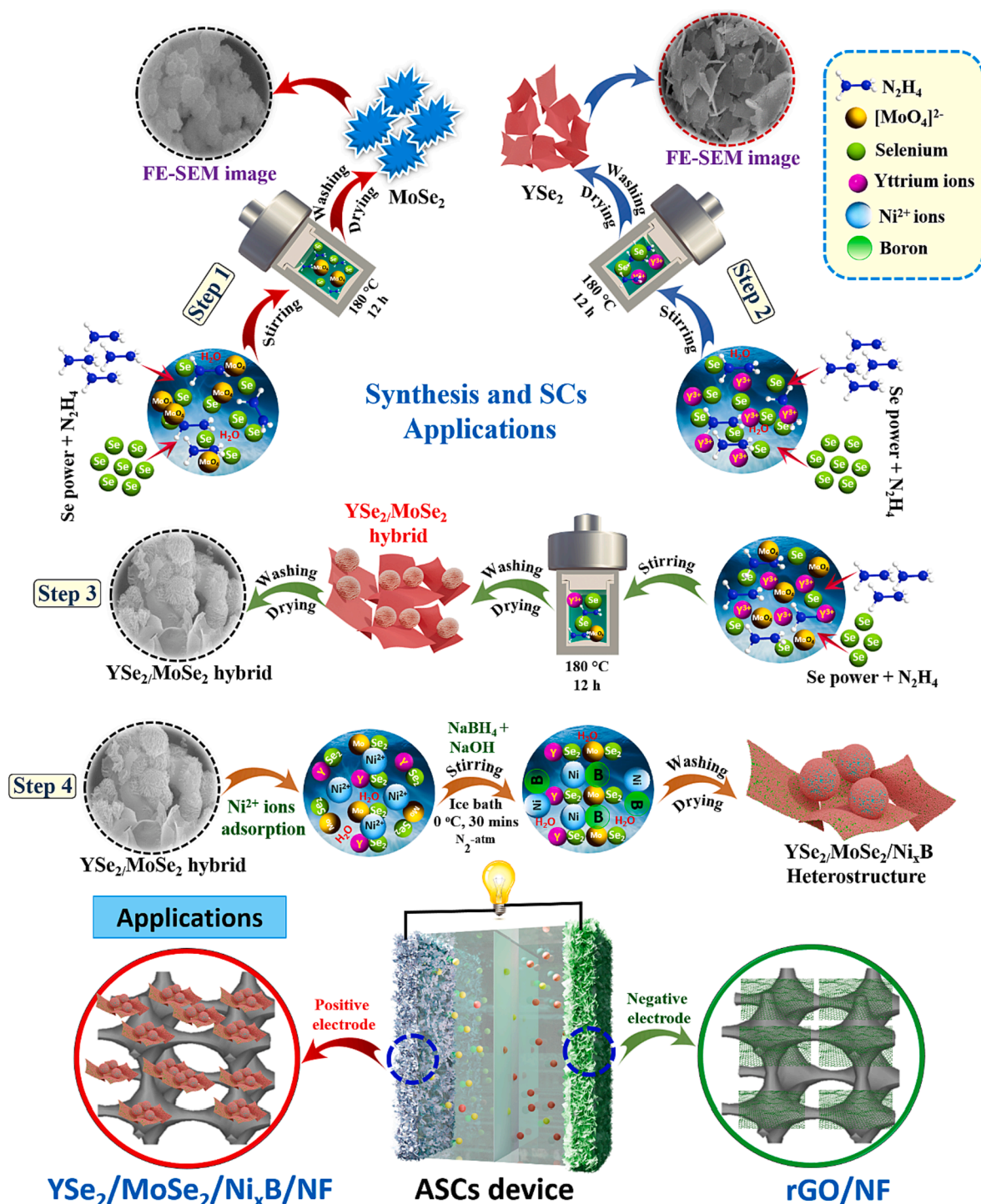
Scheme 1. The overall synthesis procedure for MoSe₂ (step 1), YSe₂ (step 2), YSe₂/MoSe₂ hybrid (step 3), and YSe₂/MoSe₂/NiₓB heterostructure (step 4) and their electrochemical applications.

electrochemical activity due to insufficient active catalytic sites [10]. To this end, several strategies have been introduced, such as (i) the introduction of dopants or (ii) the creation of heterostructures with other composites. In previous reports, doping of transition metals such as Co and Ni at the MoSe₂ basal plane showed improved electrochemical capacitive behavior by creating more active sites in the form of defects/distortions [10,11]. However, recent studies have found that the formation of a semiconducting heterostructure with MoSe₂ significantly improves the charge transfer process by modulating the electronic properties and creating a synergistic effect that enhances the exposed

active sites and capacitive behavior.

Several types of MoSe₂ heterostructures based on transition metals selenides have already been reported [12,13]. In contrast, heterostructures based on rare-earth metal selenides are still unknown. Rare-earth metal selenides such as Sm₂Se₃, CeSe₂, and La₂Se₃ have been used as electrode materials for SC due to their 4f electron configuration [14–16]. In this series, yttrium selenide (YSe₂) is rarely used as an electrode material for energy storage applications. Yttrium can increase electrical conductivity, support charge transfer, and stabilize the overall structure because the change of energy band structure can create a more
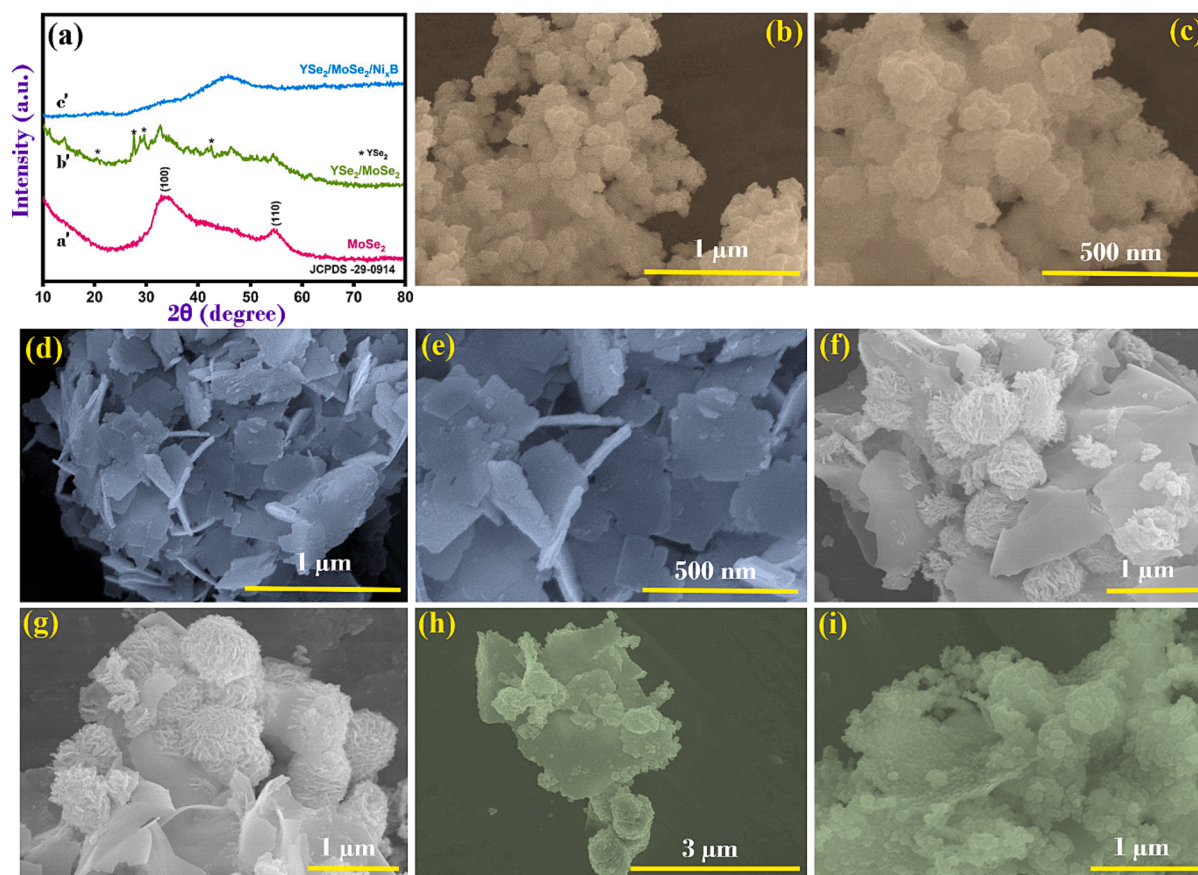
Fig. 1. (a) XRD pattern of (a') $MoSe_2$, (b') $YSe_2/MoSe_2$, and (c') $YSe_2/MoSe_2/Ni_xB$, (b, c) FE-SEM images of $MoSe_2$, (d, e) YSe_2, (f, g) $YSe_2/MoSe_2$ hybrid, and (h, i) $YSe_2/MoSe_2/Ni_xB$ heterostructure.

active site at the grain boundaries [17–19]. As a cation, it can have a maximum number of charge carriers and has a low activation energy, which enables easy electron transfer from the valence band to the conduction band by decreasing the value of the band gap and thus increasing the specific capacitance [17]. This high valence of Y associated with Se ions can increase the charge transport rate, which increases the redox properties that can affect the pseudocapacitive nature of the battery-type SC. For this reason, the creation of $YSe_2/MoSe_2$ heterostructures is a positive approach for SC and can prevent aggregation and serve as an ion buffer reservoir to facilitate the charge/discharge process [3]. To prevent structural changes during the capacitive process, an alternative is to create a rational heterostructure by integrating $YSe_2/MoSe_2$ with different components.

One suitable component is transition metal borides (TMBs). Due to their metalloid nature, they have recently been considered as an alternative energy storage material. The presence of insubstantial boron groups and a modified electronic structure lead to a low activation energy during the charge/discharge process [20,21]. From this series, nickel boride (Ni_xB) is used as an active material for constructing various heterostructures and as an electrode for SCs due to its reversible redox activity, high theoretical capacity, and selectivity [22]. In our recent studies (*Karthik and Sukanya et al.*), we introduced a combination of Ni_xB/$MnMoO_4$ hybrid electrodes and achieved a specific capacitance of 587.4 F/g along with a high Coulombic efficiency of 99.8% [23]. *Tian et al.* also constructed a ternary heterostructure based on a $NiSe_2$-Fe_3S-e_4@NiCoB electrode, which exhibited a specific capacity of 887.0C/g at 1 A/g [24]. These reports showed that the combination with Ni_xB resulted in a high capacitance rate and Columbic efficiency.

Encouraged by these studies, we now propose a new ternary heterostructure that combines the advantages of the individual components to give a hybrid with large surface areas, highly active catalytic sites,

and improved charge diffusion rates through strong synergistic effects. Herein, we have developed a heterostructure combination of yttrium diselenide/molybdenum diselenide hybrid with amorphous nickel boride nanoparticles ($YSe_2/MoSe_2/Ni_xB$), using a simple hydrothermal synthesis followed by a liquid phase route. The fabricated heterostructure combines the advantages of layered catalytic sites rich in $YSe_2/MoSe_2$ and Ni_xB with excellent electrochemical activity. It can form a coherent network with more exposed sites and provide a short ion diffusion pathway. As a result, the $YSe_2/MoSe_2/Ni_xB$ electrode exhibited a specific capacitance of 893.3 F/g at 1 A/g, and the capacitance remained at 128.17% of its original value over 5000 cycles. In addition, an aqueous asymmetric device was constructed using $YSe_2/MoSe_2/Ni_xB$ as the positive electrode and reduced graphene oxide ($YSe_2/MoSe_2/Ni_xB$//rGO) as the negative electrode. This device also showed desirable electrochemical performance in terms of a high energy density of 39.5 Wh/kg and power density of 800 W/kg.

2. Experimental section

2.1. Synthesis of $YSe_2/MoSe_2$ hybrid

The $YSe_2/MoSe_2$ hybrid was prepared according to a previously published article with slight modification [25]. In this method, 0.02 M $Na_2MoO_4·2H_2O$ and 0.02 M YCl_3 were stirred in 30 mL double-distilled (DD) water for 20 min. About 0.05 M Se powder was added to this solution and stirred again for 30 min. Then 10 mL of hydrazine monohydrate solution was slowly poured into the above solution until a black precipitate was formed. The final solution was stirred for up to 1 h to obtain a uniform precipitate. Finally, the obtained black solution was transferred to a 100-mL autoclave containing Teflon and heated in a hot-air oven at 180 °C for 12 h for the hydrothermal reaction. After that, the

solution mixture was allowed to cool at room temperature. Then the obtained product was collected and cleaned several times with DD water/ethanol and finally dried at 45 °C for 12 h.

For comparison, the pristine YSe_2 and $MoSe_2$ were prepared separately under the same temperature conditions.

2.2. Synthesis of $YSe_2/MoSe_2/Ni_xB$ heterostructure

For heterostructure synthesis, a solution (25 mL DD water) was dispersed with 50 mg $YSe_2/MoSe_2$ hybrid and stirred for up to 30 min to obtain a uniformly dispersed solution. To this aqueous mixture, 0.125 M $Ni(NO_3)_2 \cdot 6H_2O$ was added and stirred to ensure that the $YSe_2/MoSe_2$ hybrid completely adsorbed the Ni^{2+} ions. Then, 10 mL of $NaBH_4$ (0.5 M) containing 0.04 g of NaOH was added dropwise to the above solution and stirred for 30 min at a temperature of 0 °C under a nitrogen (N_2) atmosphere. The product finally obtained was centrifuged and rinsed various times with DD water/ethanol to eliminate the unsupported ions. The obtained black powder of the $YSe_2/MoSe_2/Ni_xB$ heterostructure was used for the electrochemical tests and further characterization.

For comparison, the Ni_xB NPs were also prepared by the synthesis method proposed above without introducing a $YSe_2/MoSe_2$ hybrid. The overall synthesis procedure for $MoSe_2$ (step 1), YSe_2 (step 2), $YSe_2/MoSe_2$ hybrid (step 3), and $YSe_2/MoSe_2/Ni_xB$ heterostructure (step 4) and their electrochemical applications are shown in Scheme 1. Characterization techniques and electrochemical testing of materials are listed in the supporting information (see *S2.1* and *S2.2* materials details, material characterization, and electrochemical testing).

3. Results and discussion

The formation mechanism of the $YSe_2/MoSe_2/Ni_xB$ heterostructure is shown in Scheme 1. The reaction proceeds in several steps, such as nucleation and growth, which include optimizing temperature and solution concentration. The $YSe_2/MoSe_2$ hybrid is first synthesized by a simple one-step hydrothermal approach, and its formation mechanism is based on a previously published article [25]. In the reaction, the precursors YCl_3 (Y-source) and $Na_2MoO_4 \cdot 2H_2O$ (Mo-source) first react to form an yttrium molybdenum oxide combination during core formation, followed by the reduction of Se in the presence of hydrazine. During the hydrothermal reaction (high-temperature treatment), the growth of these nuclei takes place, which finally develops into two-phase single and bulk layers of $YSe_2/MoSe_2$ hybrid. The above heterostructures were constructed based on the following considerations: (i) YSe_2 and $MoSe_2$ can be prepared simultaneously and grown in the same reaction system, which supports the development of a stable and integrated heterointerface. (ii) The $MoSe_2$ layers are grown and attached to the YSe_2 single layers to form the unique $YSe_2/MoSe_2$ hybrid. After the formation of the $YSe_2/MoSe_2$ hybrid, Ni_xB NPs are decorated on the $YSe_2/MoSe_2$ by a simple liquid phase route [23], resulting in the formation of the $YSe_2/MoSe_2/Ni_xB$ heterostructure.

The formation of the $YSe_2/MoSe_2/Ni_xB$ heterostructure was initially investigated by p-XRD analysis. Fig. 1(a) shows the corresponding XRD of $MoSe_2$, $YSe_2/MoSe_2$, and $YSe_2/MoSe_2/Ni_xB$ heterostructures. The XRD patterns confirm the successful stepwise formation of hybrid structures using simple synthesis procedures. The XRD pattern of pure $MoSe_2$ in Fig. 1(a') shows the presence of diffraction peaks at 33.71° and 54.70° corresponding to planes (1 0 0) and (1 1 0), and it is consistent with the amorphous 2D layered phases of pristine $MoSe_2$ (JCPDS No. 29-0914) [10]. However, the low intense plane (0 0 2) at 11.10° indicates the formation of multiple layers of $MoSe_2$. Indeed, the low and broad intensity peaks are mainly due to the presence of $MoSe_2$ multilayers. After the formation of the hybrid, the intensity of the XRD patterns of $MoSe_2$ is slightly increased and exhibits several peaks related to the mixed phases of the $MoSe_2$ and YSe_2 materials (Fig. 1(b')). Comparing the XRD pattern of YSe_2 in Fig. S1 with the standard reference pattern, the main diffraction peaks at 20.53°, 27.71°, 29.63°, and 42.64° can be

assigned to the tetragonal space group P4/nmm [26]. In this structure, the Y^{3+} is bound to four equivalent and five equivalent Se^{2-} atoms in a 9-coordinate geometry. The other diffraction peaks at angles of 11.13°, 14.18°, 32.82, 46.32, and 54.30° corresponding to planes (0 0 2), (1 0 2), (1 0 0), (1 0 5), and (1 1 0), respectively, are associated with the bulk phase of $MoSe_2$. The appearance of new diffraction peaks is closely related to the bulk shape of $MoSe_2$, which could be due to the layer's transformation into the bulk shape after integration with YSe_2. In addition, a shift in peak positions was observed, suggesting that the formation of a hybrid may lead to a change in crystallinity and a decrease in the size of crystallites in different dimensions or orientations. Moreover, this will affect the morphology of $MoSe_2$ after combination with YSe_2.

In addition, the variation of the diffraction angle indicates the strong synergy between YSe_2 and $MoSe_2$. The broadened full width at half maximum (FWHM) of $MoSe_2$ peaks in the $YSe_2/MoSe_2$ hybrid indicates the successful integration of $MoSe_2$ on the YSe_2 surface. No additional impurities were found, confirming the formation of a mixed phase of YSe_2 and $MoSe_2$. Finally, the formation of the targeted $YSe_2/MoSe_2/Ni_xB$ heterostructure was confirmed by the diffraction pattern in Fig. 1 (c'), which shows the presence of a wide-ranging peak at 45.68° linked with the amorphous phase of Ni_xB (consistent with Fig. S1) and also observed in the suppressed diffraction peaks of $YSe_2/MoSe_2$. This reduction in the diffraction patterns of the $YSe_2/MoSe_2$ hybrid in the final heterostructure indicates the complete coverage of the weakly crystalline Ni_xB on the surface of the $YSe_2/MoSe_2$ [23]. In addition, the shift in the 2θ value of pure Ni_xB (for Ni_xB (2θ = 45.14°)) and $YSe_2/MoSe_2$ hybrid compared to the XRD pattern of $YSe_2/MoSe_2/Ni_xB$ indicates the successful formation of the heterostructure. The XRD analysis of the $YSe_2/MoSe_2/Ni_xB$ heterostructure is consistent with the morphological results in Fig. 1(h, i). This crystallographic analysis clearly shows that the ternary $YSe_2/MoSe_2/Ni_xB$ heterostructure is formed. Following the XRD analysis, the formation of the ternary $YSe_2/MoSe_2/Ni_xB$ heterostructure was further elucidated by predicting molecular vibrations using Raman analysis. Fig. S2 shows the corresponding Raman spectra of the $YSe_2/MoSe_2$ hybrid, $YSe_2/MoSe_2/Ni_xB$ heterostructure, which indicates the presence of both vibrational modes of $YSe_2/MoSe_2$ and Ni_xB by showing a broad peak in the range of 200–1200 cm^{-1} [23]. The Raman shifts at 366, 806.9, and 1020.4 cm^{-1} are among the corresponding features of the binding of $YSe_2/MoSe_2$ [26,10]. Moreover, a broad peak at a higher Raman shift indicates the successful incorporation of amorphous Ni_xB into the $YSe_2/MoSe_2$ hybrid [23].

The surface morphology and texture of the formed ternary $YSe_2/MoSe_2/Ni_xB$ were systematically analyzed using FE-SEM (Fig. 1(b–i)) and FE-TEM. Fig. 1(b, c) shows the high and low magnification FE-SEM images of pristine $MoSe_2$ with 2D multilayers. The multilayers are interconnected and appear as a flower-like structure. Fig. 1(d, e) shows the presence of unfolded sheet structured YSe_2 interconnected in the form of arrays. The sheets' surface is smoother, indicating enhanced crystallinity and the interconnected gaps are helpful for ion transport during the electrochemical process. In addition, the surface morphology of the $YSe_2/MoSe_2$ hybrid combination was demonstrated and shown in Fig. 1(f, g). It can be clearly seen that YSe_2 is in the form of 2D layers with a thin surface (compared to untreated YSe_2), which are anchored with several multi-layers of $MoSe_2$. From the image, it can be inferred that the $MoSe_2$ layers are arranged like a lamellar structure with intertwined nanosheet subunits and are gently attached to both sides of the thin YSe_2 sheets with a smooth surface (Fig. 1(f, g)), which are bent and folded. This covering largely prevents the aggregation of $MoSe_2$ and its stacking in the hybrid structure. Moreover, Fig. 1(f, g) shows that the flower-like $MoSe_2$ layers are irregularly embedded in the YSe_2 layers. Furthermore, the $MoSe_2$ units are positioned on the YSe_2 with abundantly exposed edges, forming a coherent network structure. The obtained morphology indicates that the 2D-2D structure possesses numerous catalytically active sites that could enhance the
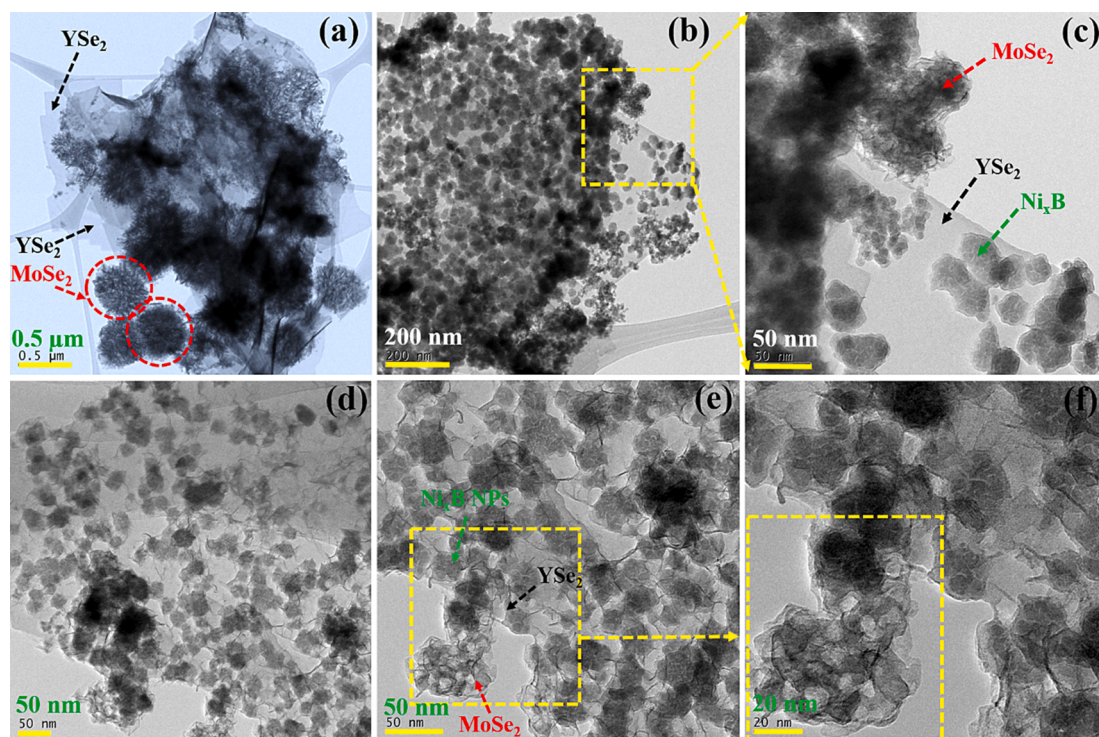
Fig. 2. Different magnifications (low/high) of FE-TEM images of (a) YSe$_2$/MoSe$_2$ and (b-f) YSe$_2$/MoSe$_2$/Ni$_x$B heterostructures.

electrochemical response for energy storage applications. Followed by this, the pristine Ni$_x$B appears as nanoparticles with a more agglomerated structure, as shown in Fig. S1(a–c) (FE-SEM and TEM images). After the introduction of Ni$_x$B, the morphology in Fig. 1(h, i) shows that the 2D/2D layers of the YSe$_2$/MoSe$_2$ hybrid are completely enveloped with Ni$_x$B NPs (in agreement with XRD) and that these enveloping Ni$_x$B prevent them (YSe$_2$/MoSe$_2$) from agglomerating during synthesis. In addition, the high-resolution image shows that the Ni$_x$B is fully embedded in the YSe$_2$/MoSe$_2$ hybrid. MoSe$_2$ is invisible in some areas

(consistent with XPS) because the YSe$_2$/MoSe$_2$ hybrid is completely covered by Ni$_x$B NP, showing the strong synergy of Ni$_x$B with the 2D-structured YSe$_2$/MoSe$_2$ hybrid.

In addition, structural features and morphological changes were assessed using FE-TEM analysis. Fig. 2(a–f) shows the corresponding FE-TEM images with different magnifications of the YSe$_2$/MoSe$_2$ hybrid and the YSe$_2$/MoSe$_2$/Ni$_x$B heterostructure. They show the formation of the hybrid structure and also the complete decoration of the Ni$_x$B NP on the thin layer surface of the YSe$_2$/MoSe$_2$ hybrid. Fig. 2(a) shows that the
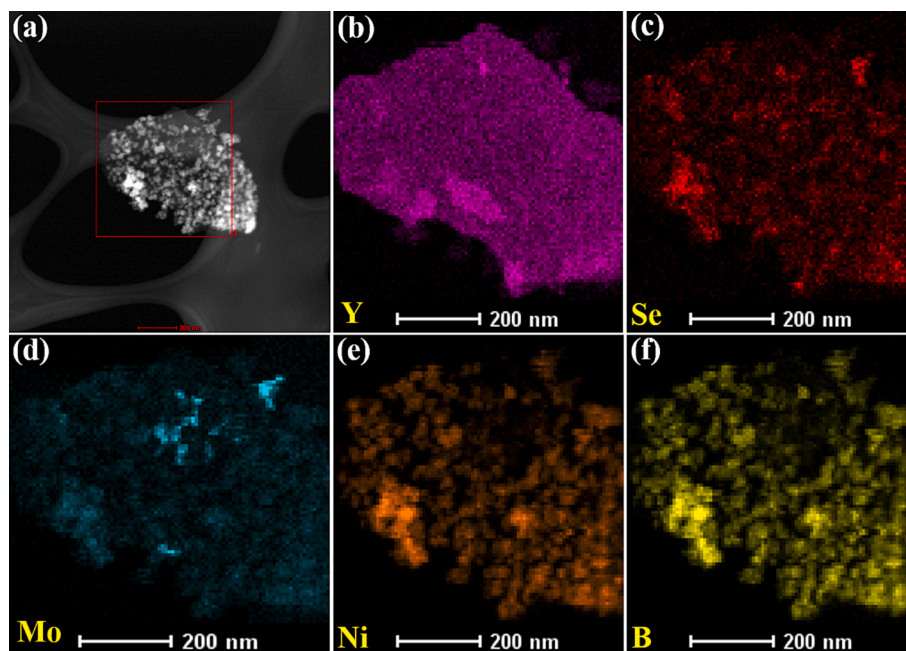

Fig. 3. (a) STEM-HADDF resolved dark field image and area scan mapping images of YSe$_2$/MoSe$_2$/Ni$_x$B heterostructure: (b) yttrium (Y), (c) selenium (Se), (d) molybdenum (Mo), (e) nickel (Ni), and (f) boron (B).
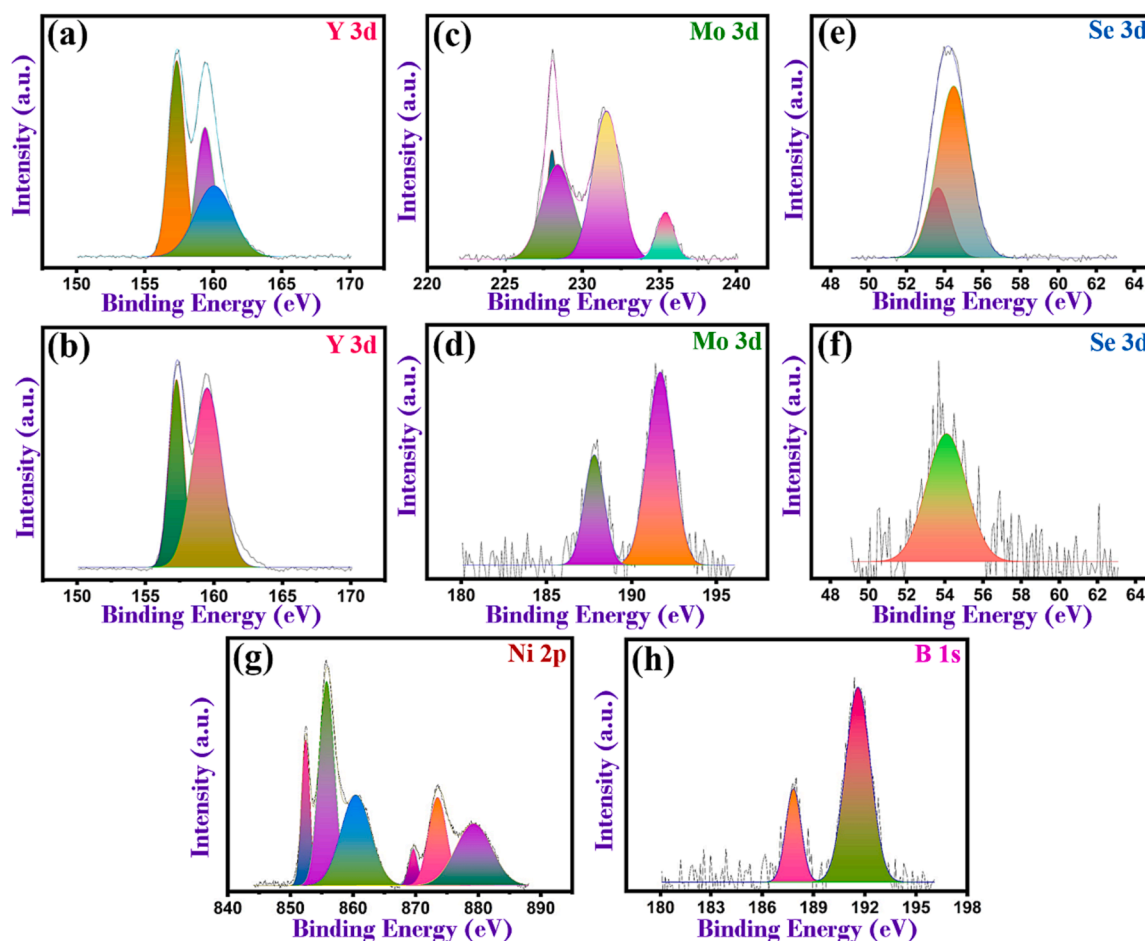
Fig. 4. Individual scan spectra of the (a) Y 3d, (c) Mo 3d, (e) Se 3d in YSe$_2$/MoSe$_2$ hybrid and (b) Y 3d, (d) Mo 3d, (f) Se 3d, (g) Ni 2p and (h) B 1s in YSe$_2$/MoSe$_2$/Ni$_x$B heterostructure.

YSe$_2$ is in the form of transparent and thin individual layers that are folded and bent like 2D materials. These thin layers are decorated and randomly connected with multiple layers of flower-like structured MoSe$_2$ sheets. The high-resolution images of the YSe$_2$/MoSe$_2$ hybrid are shown in Fig. S4. Apart from the hybrid layer, the YSe$_2$ appeared and retained a very thin layer of 2D nanosheets even after the introduction of Ni$_x$B, as shown in Fig. 2(b–f), and it also has more active sites and serves as binding sites for both MoSe$_2$ and Ni$_x$B. These ultrathin surfaces of YSe$_2$ sheets with numerous catalytic sites could support the rapid transport of ions through the electrolyte during the energy storage process. The high-resolution image in Fig. 2(c) clearly shows that the Ni$_x$B NPs randomly adhere to the basal surface of the MoSe$_2$ multilayer and are fully decorated on the YSe$_2$ thin sheets. This may cause the MoSe$_2$ multilayer planes to break and spread over the YSe$_2$ sheets, as shown in Fig. 2(d, e), demonstrating the non-uniform coverage of the MoSe$_2$ layers on the thin YSe$_2$ edges and basal surfaces. This layer breakage and random arrangement of MoSe$_2$ is mainly caused by introducing the reducing agent NaBH$_4$, which can reduce the MoSe$_2$ again during heterostructure formation. More importantly, the complete coverage of Ni$_x$B NPs on both MoSe$_2$ and YSe$_2$ layers was clearly indicated by the high-resolution image in Fig. 2(e, f), and this complete coverage by Ni$_x$B also helps to prevent the agglomeration of the YSe$_2$/MoSe$_2$ hybrid, which is consistent with the result of FE-SEM analysis. The high-resolution, magnified lattice image in Fig. S3 shows the combinations of ultrathin YSe$_2$ and hierarchically layered MoSe$_2$ nanosheets covered with Ni$_x$B NPs, forming a ternary heterostructure interface. More details about the lattice structure and SAED pattern of the YSe$_2$/MoSe$_2$/Ni$_x$B heterostructure can be found in the Supporting Information

(Fig. S3).

To confirm the decoration of Ni$_x$B on the YSe$_2$/MoSe$_2$ hybrid, the high-angle annular dark-field images (HADDF-STEM) and area scan mapping were performed. The corresponding HADDF-STEM image in Fig. 3(a) confirms the presence of the YSe$_2$/MoSe$_2$/Ni$_x$B heterostructure in the form of a dark-field-resolved image. In addition, the area mapping images of all elements are shown in Fig. 3(b–f). Elements such as Y, Mo, Se, Ni, and B were clearly detected on the mapping site. This result proves the formation of a ternary YSe$_2$/MoSe$_2$/Ni$_x$B heterostructure with uniform distribution of all elements in a reasonable ratio. We also compared the elemental distribution and HR-TEM images (Fig. S4(a–c)) of each component (YSe$_2$/MoSe$_2$) using HADDF-STEM analysis to confirm the presence of pristine Y (e), Mo (f), and Se (g) in the 2D system (Fig. S4).

The details about the chemical state and the components present in the synthesized YSe$_2$/MoSe$_2$ hybrid and ternary YSe$_2$/MoSe$_2$/Ni$_x$B heterostructure were investigated by XPS analysis. The XPS results show that the atomic weight percentage of elements Y, Mo, Se, Ni, and B in the heterostructure varies after introducing Ni$_x$B compared to YSe$_2$/MoSe$_2$. The corresponding percentages are shown in Table S1. To confirm this phenomenon, the XPS survey and high-scan spectra are plotted to determine the differences in the elemental state. The survey spectra for YSe$_2$/MoSe$_2$ hybrid and YSe$_2$/MoSe$_2$/Ni$_x$B heterostructure are shown in Fig. S5 and confirm the presence of Y, Mo, Se, Ni, and B in the hybrid. From the individual scan spectra of Y in YSe$_2$/MoSe$_2$ (Fig. 4(a)), it is evident that there are three well-defined deconvoluted peaks at binding energies of 157.3, 159.8, and 160.9 eV associated with the Y^{3+} oxidation state of the corresponding subshells 3d$_{5/2}$ and 3d$_{3/2}$, respectively [27].
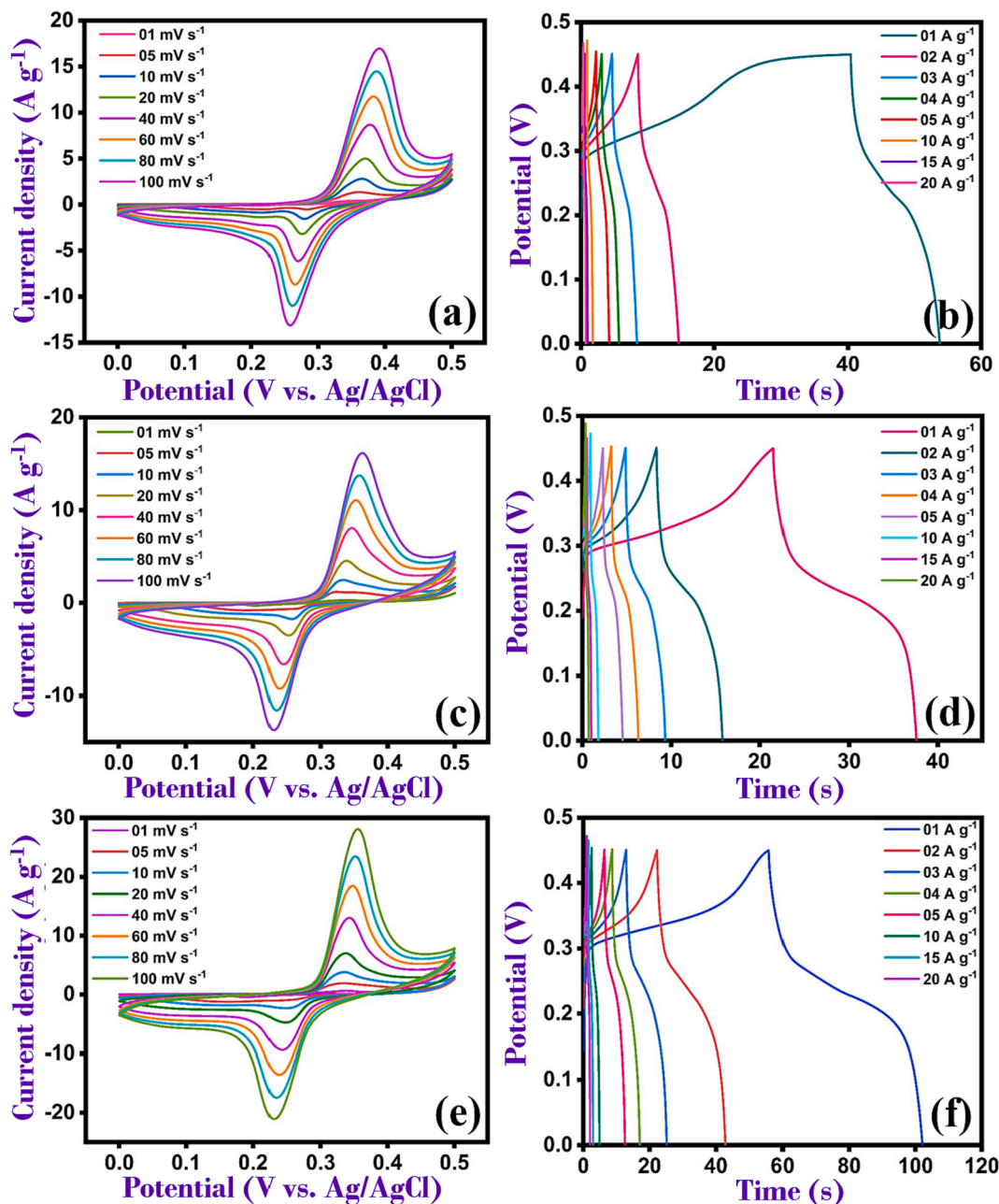
Fig. 5. CVs recorded at varying scan rates from 1 to 100 mV s^{-1} and GCDs recorded at current densities applied from 1 to 20 A/g in 3 M KOH for MoSe$_2$ ((a) and (b)), YSe$_2$ ((c) and (d)) and YSe$_2$/MoSe$_2$ hybrid ((e) and (f)).

However, in the case of the ternary heterostructure (Fig. 4(b)), the peak intensity and area of Y 3d$_{5/2}$ are reduced and slightly shifted to a binding energy of 0.1 eV with the absence of a peak at 160 eV, confirming the change in the chemical and physical state of Y after the incorporation of Ni$_x$B. In the case of the Mo spectrum (Fig. 4(c)), the peaks of the Mo^{4+} 3d$_{5/2}$ and Mo^{4+} 3d$_{3/2}$ levels, related to binding energies of 231.6 and 228.4 eV, can be seen as doublets. Then, the Mo spectrum shows an additional peak at 235.6 and 228 eV, indicating the presence of Mo^{6+} 3d$_{5/2}$ in the hybrid structure [10]. Moreover, this result confirms the presence of multivalent Mo ions in the hybrid system, which obviously leads to high electrical conductivity. However, in the heterostructure, the Mo spectrum (Fig. 4(d)) contains only one singlet peak of Mo^{6+} 3d$_{5/2}$ and Mo^{4+} 3d$_{5/2}$, indicating that the phase changes after the introduction of Ni$_x$B. The Se spectra in (Fig. 4(e)) show the presence of doublet peaks at a binding energy of 54.4 and 53.6 eV, corresponding to the Se 3d$_{5/2}$ and Se 3d$_{3/2}$ subshells of the metal selenide bonds in the YSe$_2$/MoSe$_2$

hybrid [10]. However, a similar phenomenon of reduction of the Se peak with a broad area was observed in the ternary heterostructure (Fig. 4(f)), indicating the presence of a Se 3d$_{5/2}$ subshell peak at a binding energy of 54.7 eV. To confirm the presence of Ni$_x$B in YSe$_2$/MoSe$_2$/Ni$_x$B, the individual scan spectra of Ni and B were fitted and are shown in Fig. 4(g, h). The Ni spectrum shows multiple peaks at binding energies of 873.5 eV and 855.8 eV associated with the Ni^{2+} 2p$_{1/2}$ and Ni^{2+} 2p$_{3/2}$ oxidation states. The existence of a metallic nickel phase (Ni^0) on the final heterostructure was observed at a binding energy of 869.6 and 852.8 eV, respectively. Subsequently, additional peaks of Ni species (satellite) occurred at a binding energy of 879.3 eV and 860.4 eV related to Ni^{2+} states. The B species in the final hetero system shows two prominent peaks at a binding energy of 191.6 and 187.8 eV, respectively [23]. The shift in the binding energy of the element boron plays a vital role in electron transport to enhance the electrochemical activity and energy storage mechanism. In this case, the element boron has shifted to a
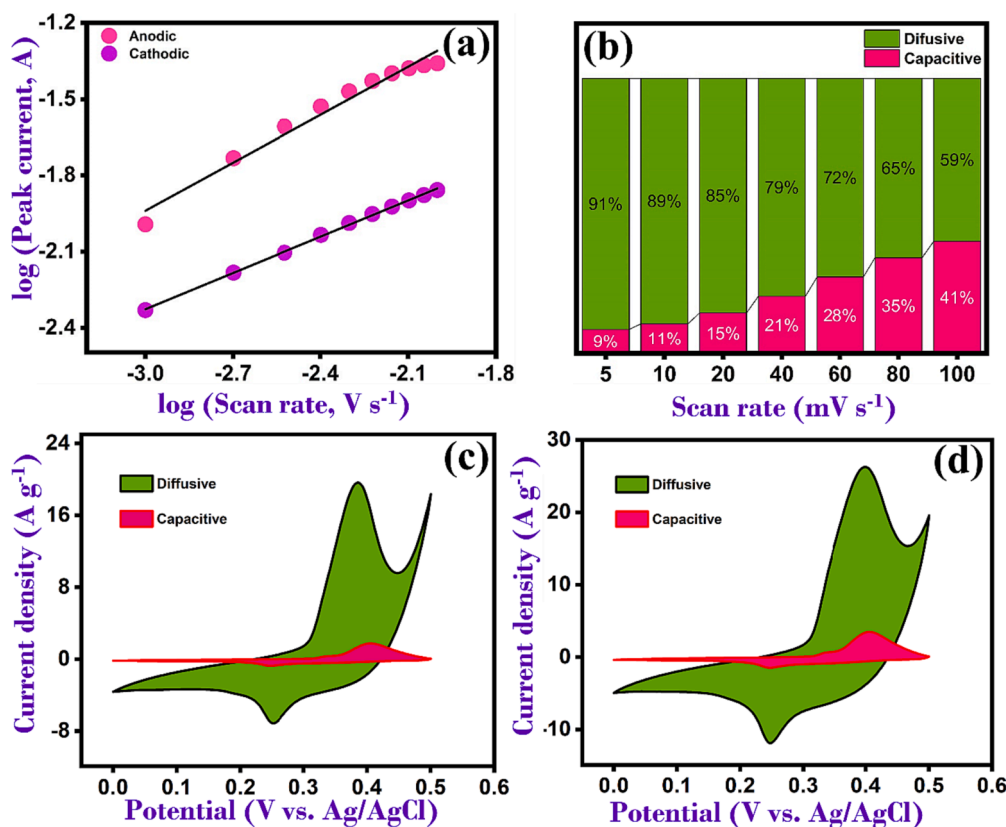
Fig. 6. (a) Logarithm of peak current as a function of the logarithm of scan rate, (b) contribution of diffusive and capacitive contributions as a function of scan rate, and (c) and (d) CVs with highlighted diffusive and capacitive contributions recorded at 5 and 10 mV s^{-1}.
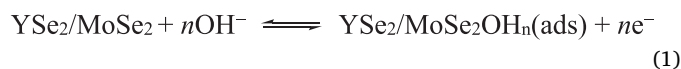
higher value, which means the reverse transport of electrons from B to Ni and increases electron density around Ni, which may lead to a change in the electronic structure of the whole system. Moreover, the XPS results confirm that the incorporation of Ni$_x$B into YSe$_2$/MoSe$_2$ causes significant changes in the phase and electronic structure of the entire ternary heterostructure system. In addition to the XPS results, the percentage of elements Y, Mo, and Se in the hybrid was also calculated by ICP-AES analysis. The results are shown in Table S1. From the result, the ratio of Y (0.17 %), Mo (0.16 %) and Se (2.96 %) is 1:1:2, which is related to the experimental error and counted as 1:1:2 ratio in the final YSe$_2$/MoSe$_2$. The ICP results are slightly different from the values calculated by XPS. Since XPS is a surface analysis, it does not provide depth results for the percent analysis of the sample. However, the result from ICP-AES confirms the combination of YSe$_2$ and MoSe$_2$ in the final hybrid.

4. Electrochemical characterization and performance

The electrochemical properties of MoSe$_2$, YSe$_2$, and YSe$_2$/MoSe$_2$ were investigated using cyclic voltammetry (CV) and galvanostatic charge/discharge analysis (GCD), and these data are summarized in Fig. 5(a–f). For the CV measurements (Fig. 5(a), (c), and (e)), the scan rate was varied from 1 to 100 mV s^{-1} between the potentials of 0.0 and 0.5 V versus Ag/AgCl in 3 M KOH. The CV plots for MoSe$_2$, YSe$_2$, and YSe$_2$/MoSe$_2$ are similar and show quasi-reversible redox behavior. The peak-to-peak separation is high for MoSe$_2$, reaching 0.14 V at 100 mV s^{-1}, which might be related to the resistance to internal diffusion of electrolyte OH$^-$ ions [28], and the insufficient access to MoSe$_2$ at the higher scan rates limits its capacity. A slightly lower value of 0.13 V is obtained for YSe$_2$, while the lowest value of 0.11 V (at 100 mV s^{-1}) is obtained with YSe$_2$/MoSe$_2$. These data indicate faster ion/electron transport and more efficient redox reactions for YSe$_2$/MoSe$_2$. In

addition, the integrated charge associated with the redox peaks is significantly higher for YSe$_2$/MoSe$_2$, indicating a much higher specific capacitance of this hybrid than MoSe$_2$ or YSe$_2$. The presence of Y increases the electrical conductivity and helps to reduce the resistivity effect during the cycling process.

Similar quasi-reversible redox behavior is seen in YSe$_2$ and the YSe$_2$/MoSe$_2$ hybrid, and this is consistent with the intercalation of ions across the nickel foam (NF) and YSe$_2$ with an enhanced current density in the highly alkaline electrolyte medium. In general, the central metal cation (M$^+$) in the hybrid (YSe$_2$/MoSe$_2$) or single material (MoSe$_2$) and their related M/M−OH reaction confirms the presence of reversible faradic redox reaction and results in enhanced specific capacitance [29–31]. In particular, the redox peaks observed in MoSe$_2$ can be attributed to the reversible conversion of Mo (IV) to Mo (VI) [32], and this process probably also occurs in YSe$_2$/MoSe$_2$, and is related to the faradic redox reaction as described in Eqs. (1) and (2).

$$\text{YSe}_2/\text{MoSe}_2 + n\text{OH}^- \rightleftharpoons \text{YSe}_2/\text{MoSe}_2\text{OH}_n(\text{ads}) + n\text{e}^-$$
(1)

$$\text{MoSe}_2 + n\text{OH}^- \rightleftharpoons \text{MoSe}_2\text{OH}_n(\text{ads}) + n\text{e}^- \quad (2)$$

The corresponding GCD tests are summarized in Fig. 5(b), (d), and (f) for MoSe$_2$, YSe$_2$, and YSe$_2$/MoSe$_2$, respectively. These tests were done at various current densities from 1 to 20 A/g in the range of 0.0 to 0.45 V. The YSe$_2$ and YSe$_2$/MoSe$_2$ curves show nonlinear responses with distinct potential plateau regions characteristic of the faradaic process and battery-like activity. The GCD curves are less symmetric for MoSe$_2$, possibly due to less reversible OH$^-$ reaction kinetics during the electrochemical redox reaction. The specific capacitance was determined by applying Eq. (3), where I is the current response, ΔV is the potential window, Δt is the time for discharge, m is the mass, and C_s is the specific capacitance. The C_s values were calculated as 29.44 F/g, 35.67 F/g, and
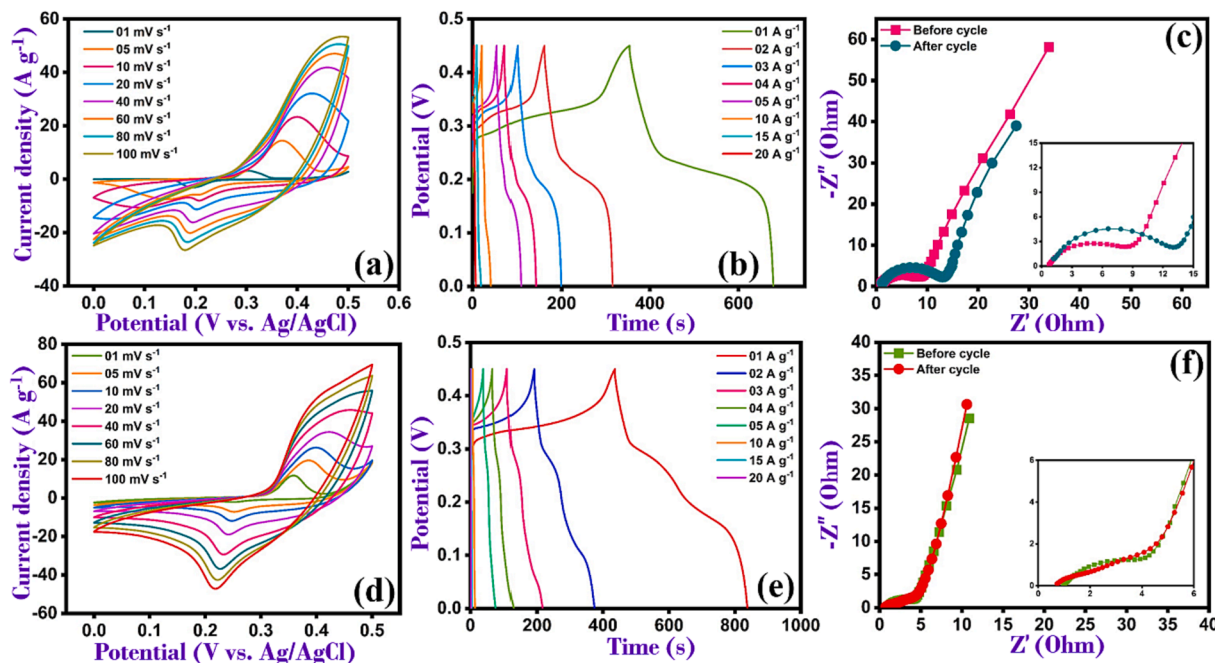
Fig. 7. CVs recorded between 0.0 and 0.5 V vs. Ag/AgCl at scan rates of 1 and 100 mV s^{-1}, GCDs recorded at current densities from 1 to 20 A/g, and electrochemical impedance data for Ni$_x$B ((a), (b), and (c)) and the YSe$_2$/MoSe$_2$/Ni$_x$B ((d), (e) and (f)).

102.67 F/g at 1 A/g and 15.56 F/g, 15.50 F/g, and 44.44 at 20 A/g for MoSe$_2$, YSe$_2$, and YSe$_2$/MoSe$_2$, respectively.

In addition, the C_s values for other corresponding current densities are given in Fig. S6. It can be seen from this comparison that YSe$_2$/MoSe$_2$ has the greatest potential for high capacitance.

$$C_s = \frac{I\Delta t}{m\Delta V} \tag{3}$$

To further improve the ease of OH$^-$ ions access throughout the charge/discharge process, amorphous Ni$_x$B was chosen as an additional component and combined with the YSe$_2$/MoSe$_2$ to form a YSe$_2$/MoSe$_2$/Ni$_x$B hybrid. The amorphous Ni$_x$B was selected because it has more pores and a larger active surface area and is effective in fabricating an asymmetric supercapacitor [23]. Fig. 7(a, d) compares the performance of Ni$_x$B and the YSe$_2$/MoSe$_2$/Ni$_x$B hybrid. In Fig. 7(a), the CVs are plotted as a function of the scan rate for Ni$_x$B (1–100 mV s^{-1}) and show a pair of well-defined redox peaks, again indicating a quasi-reversible response with the intercalation/deintercalation of OH$^-$ ions [23]. The redox events can be attributed to the oxidation of Ni^{2+} in Ni$_x$B to Ni^{3+}, while the reverse reduction wave is associated with the conversion of Ni^{3+} back to Ni^{2+} (Ni(OH)$_2$ + OH$^-$ ⇌ NiOOH + H$_2$O) [33]. Moreover, the current density was observed to increase linearly with an increase in the scan rate, indicating a fast faradic response. Similar data are shown for the YSe$_2$/MoSe$_2$/Ni$_x$B hybrid (Fig. 7(d)), but in this case, better-resolved redox peaks are seen, and the charge associated with the peaks is higher than that observed for Ni$_x$B and much higher than that observed for YSe$_2$/MoSe$_2$ (Fig. 5(f)). At the same time, a shift of the anodic and cathodic peak potentials towards more positive and negative values was observed at greater scan rates, which could be due to the increased interfacial resistance that could limit the diffusion of ions during fast cycling. However, no other significant changes in the symmetry of the CV traces were observed, even at scan rates of high value, indicating the better reversible property of the electrode leading to improved capacitive performance of YSe$_2$/MoSe$_2$/Ni$_x$B. This CV result suggests a diverse electrochemical behavior and reaction kinetics due to the strong synergism between YSe$_2$/MoSe$_2$ and Ni$_x$B and the formation of intense heterointerfaces.

To obtain information on the mechanism of the energy storage

process for YSe$_2$/MoSe$_2$/Ni$_x$B, the data from CV were further analyzed to gain insight into the role of diffusion-controlled and capacitive processes. To determine the contribution of these processes, the power law in equation (4) was used [34]. Here, i corresponds to the peak current density, v represents the scan rate, and a and b are variable parameters. The magnitude of b is related to the nature of charge storage, where a value of 0.5 designates a perfect diffusion-controlled process associated with electrolytic ion intercalation and deintercalation, while a value of 1.0 indicates a surface-controlled capacitive process (double-layer capacitance and pseudocapacitance). Taking the logarithm of equation (4), b is obtained by plotting the logarithm of i as a function of the logarithm of v. A typical plot is shown in Fig. 6(a). The linear regression equations were determined as $i = -0.05 + 0.63 \log v$ for the oxidation peaks and $i = -0.9 + 0.48 \log v$ for the reduction waves. The calculated b values of 0.48 and 0.63 indicate that this is mainly a diffusion-controlled process. Nevertheless, some element of a capacitive process exists, suggesting a combination of a diffusion-controlled and a capacitive-dominated process. The capacitive and diffusion-controlled processes contribution was further analyzed using equation (5), where $a_1 v$ and $a_2 v^{1/2}$ correspond to the capacitive and diffusion-controlled processes, respectively. The values of a_1 and a_2 were obtained by plotting the peak currents as a function of v and $v^{1/2}$, respectively.

$$i = av^b \tag{4}$$

$$i = a_1 v + a_2 v^{1/2} \tag{5}$$

The CV was deconvoluted into the diffusive and capacitive contributions using equation (5) and the calculated a_1 and a_2 terms. These data are shown in Fig. 6(b) and Fig. S7 and clearly indicate that the capacitive contribution improves with a raising scan rate, reaching 41% at 100 mV s^{-1}. This is also evident in the representative voltammograms in Fig. 6(c) and (d), where the capacitive current makes a smaller contribution to the voltammogram. This analysis shows that the charge storage capacity is primarily dominated by a diffusion-controlled process, with the intercalation and deintercalation of OH$^-$ ions.

Comparing the GCD curves in Fig. 7(b) and (e), it is clear that both the Ni$_x$B and the YSe$_2$/MoSe$_2$/Ni$_x$B exhibit high capacitance. In fact, the specific capacitance at a current density of 1 A/g was determined to be

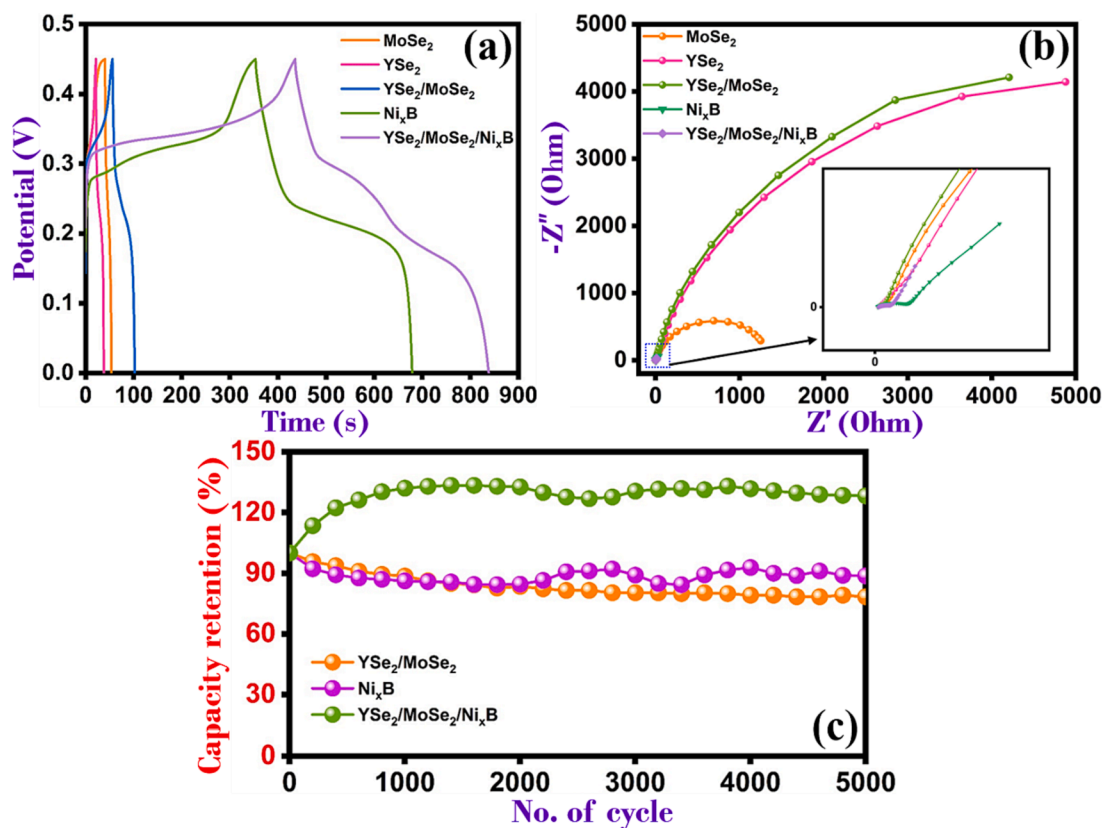**Fig. 8.** (a) GCD curves plotted at 1 A/g current density and (b) impedance data for $MoSe_2$, YSe_2, $YSe_2/MoSe_2$ hybrid, Ni_xB and $YSe_2/MoSe_2/Ni_xB$ heterostructure and (c) capacity retention plotted as a function of cycle number for $YSe_2/MoSe_2$, Ni_xB and $YSe_2/MoSe_2/Ni_xB$.

723.33 F/g for Ni_xB and 893.33 F/g for $YSe_2/MoSe_2/Ni_xB$, showing the significant increase in specific capacitance by combining $YSe_2/MoSe_2$ and Ni_xB in a hybrid. Interestingly, there are two plateau regions in the $YSe_2/MoSe_2/Ni_xB$ heterostructure during discharge, which may indicate a multiphase transition where the rate of deintercalation and stripping of OH^- on the $YSe_2/MoSe_2$ and Ni_xB phases in the heterostructure may be different. The specific capacitance for other current densities 2, 3, 4, 5, 10, 15, and 20 A/g was estimated to be 810.67, 706.67, 560.89, 416.67, 151.11, 66.67, and 31.11 F/g, respectively (Fig. S6). This trend of decreasing the specific capacitance of the $YSe_2/MoSe_2/Ni_xB$ electrode is obviously due to the fact that the OH^- ions do not have enough time to diffuse or migrate into the electrode materials. However, the obtained results prove that the proposed electrode based on the ternary material ($YSe_2/MoSe_2/Ni_xB$) has much better electrochemical storage performance than the previously reported $MoSe_2$ works, which include $MoSe_2$-C composites (876 F/g) [35], $Ni_{0.85}Se$-$MoSe_2$ (774 F/g) [3], $MnSe_2@$-$MoSe_2$ (719 F/g) [36], and $MoSe_2$-rGO (211 F/g) [37]. The results from GCD show that the Ni_xB-decorated $YSe_2/MoSe_2$ hybrid exhibits significantly improved electrochemical behavior in terms of higher specific capacitance as well as high capability rate due to the strong synergistic effect between all components (YSe_2, $MoSe_2$, and Ni_xB), which provides high electrical conductivity and redox properties that progresses the ease of electrolyte ions access during the electrochemical process. In addition, the improved specific capacitance and rate performance of the $YSe_2/MoSe_2/Ni_xB$ electrode is further explained by the following phenomena: (i) the coexistence of the electrochemically active species Ni and Mo can contribute to faradaic reversible reactions, which can be helpful for the improvement of the overall capacitance; (ii) the well-defined thin and multilayer arrays on the NF with the large surface area can expose extra catalytically active sites, reduce the ion diffusion paths and provide suitable networks for fast electron/ion transfer, resulting in improved rate capability; and finally, (iii) the presence of a

$YSe_2/MoSe_2$ heterointerface between Ni_xB modulates the electronic properties and increases the charge diffusion rate, leading to improved energy storage performance.

Electrochemical impedance spectroscopy (EIS), widely used in energy storage analysis, was employed to obtain additional information (conductivity and kinetic mechanism) about $YSe_2/MoSe_2/Ni_xB$. The impedance data are shown in Fig. 7(c, f) for the Ni_xB and $YSe_2/MoSe_2/Ni_xB$ electrodes, respectively. These data were recorded between 0.01 and 100 kHz with an AC perturbation of 10 mV. In both cases, semi-circles can be seen at high frequencies, followed by linear or near-linear regions at lower frequencies. The appearance of the semicircles may be associated with charge transfer events or faradaic reactions. The slope of the linear region is higher for the $YSe_2/MoSe_2/Ni_xB$ electrode, indicating that the phase angle (φ) is closer to an ideal capacitor with a phase angle of $-90°$. For the Ni_xB electrode, the deviation is much larger due to frequency dispersion phenomena. In addition, the semi-circle diameter region, indicating the degree of the charge transfer resistance (R_{ct}) is smaller for the $YSe_2/MoSe_2/Ni_xB$ electrode than for the Ni_xB electrode, indicating higher conductivity and making the hybrid more suitable for redox reactions. The impedance data were fitted to an equivalent circuit with a solution resistor (R_s), and an RC pair consisting of R_{ct} and capacitance (C). Using the fitted data, R_{ct} was determined to be 7.53 Ω for Ni_xB, while a lower value of 2.71 Ω was determined for the $YSe_2/MoSe_2/Ni_xB$ electrode. Similarly, a higher capacitance was calculated for the heterostructure, with values of 723.33 F/g and 893.33 F/g for the Ni_xB and $YSe_2/MoSe_2/Ni_xB$ electrodes, respectively.

Impedance data were also recorded after 5000 charge/discharge cycles to evaluate stability. These data are shown in Fig. 7(c, f) and compared with the materials before the cycles. Good stability can be seen for Ni_xB. However, the impedance values for the $YSe_2/MoSe_2/Ni_xB$ hybrid (R_{ct} = 2.83 Ω) are nearly identical before and after 5000 cycles,
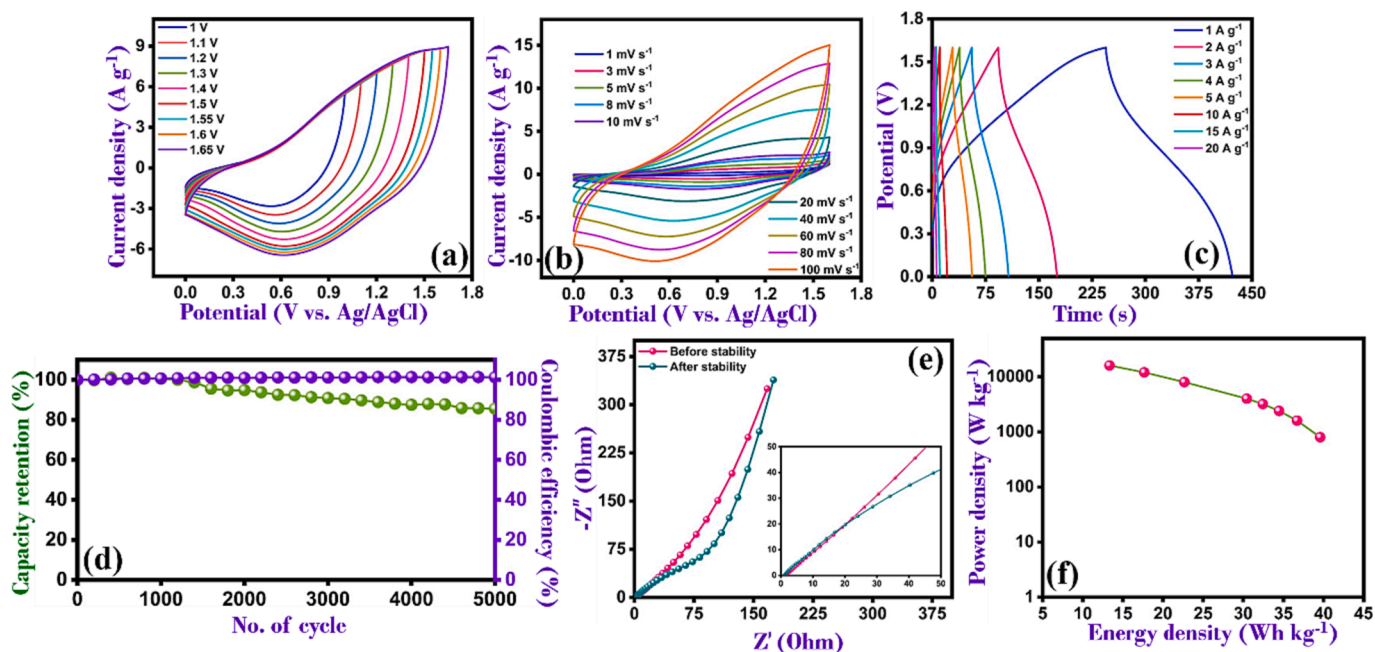
Fig. 9. (a) CVs recorded from 0.0 V to various upper potential limits. (b) CV traces were recorded at various sweep rates (1, 3, 5, 8, 10, 20, 40, 60, 80, and 100 mV/s). (c) GCD curves recorded at different current densities from 1 to 20 A/g, (d) capacity retention and Coulombic efficiency plotted as a function of cycle number for the $YSe_2/MoSe_2/Ni_xB||rGO$ device. (e) Electrochemical impedance spectroscopy and (f) Ragone plot with a power density as a function of energy density.

indicating excellent stability. This highlights the remarkable properties of the heterostructure, including stability, high capacitance, conductivity, and efficient redox activity. This is also evident in Fig. 8(a–c), which compares the GCD, impedance data, and capacitance retention for the different metal selenides and the $YSe_2/MoSe_2/Ni_xB$ heterostructure. From the comparison of these data, it can be seen that the coupling of $MoSe_2$ ($R_{ct} = 17.62$ Ω) with YSe_2 leads to a moderate increase in capacitance but causes an increase in charge transfer resistance due to the improvement in charge carrier transport after the introduction of YSe_2 ($R_{ct} = 13.5$ Ω). The Ni_xB exhibits an excellent specific capacitance (723.3 F/g) with a relatively low charge transport resistance ($R_{ct} = 8.01$ Ω). This could be due to the small particle size, which can facilitate charge transport within short diffusion paths, increasing OH^- accessibility during the charge/discharge process. However, when Ni_xB is coupled with $YSe_2/MoSe_2$, low charge transfer resistance and impressive capacitance (893.33 F/g) can be achieved, as shown by the GCD curves and impedance data (Fig. 8(a) and (b)). Another important parameter is the excellent stability associated with capacitance retention during prolonged charging and discharging. As mentioned earlier, the increase in specific capacitance of $YSe_2/MoSe_2/Ni_xB$ compared to other electrodes is due to the strong synergism between the $YSe_2/MoSe_2$ and Ni_xB components. Fig. 8(c) shows that the $YSe_2/MoSe_2/Ni_xB$ exhibits a stable and nearly constant capacitance, extending from about 500 to over 5000 cycles at 10 A/g of applied current density. The initial slight increase during the first 500 cycles could be due to the formation of more active sites, such as NiOOH. The $YSe_2/MoSe_2/Ni_xB$ electrode retained a capacitance of 128.17% after 5000 cycles. On the other hand, a significant decrease in capacitance was observed for both $YSe_2/MoSe_2$ and Ni_xB, with a 78.42% decrease in capacitance after 2000 cycles for $YSe_2/MoSe_2$ and an 88.87% decrease for Ni_xB. This indicates that the repeated intercalation and depletion of electrolytic OH^- ions lead to stresses and changes in the structural integrity of the active sites in these individual materials. This is not the case for heterostructure, highlighting its higher stability. These ideal results confirm that $YSe_2/MoSe_2/Ni_xB$ is an excellent candidate for the fabrication of ASC devices.

To better understand the electrochemical energy storage mechanism of the $YSe_2/MoSe_2/Ni_xB$ electrode after the cyclic stability test, an FE-SEM analysis was performed based on the previously published SCs

articles [38–40]. The corresponding FE-SEM image after the 5000-cycle test is shown in Fig. S8. It shows that the electrodes retain their original structure even after a number of charge/discharge cycles in a strongly alkaline environment, which means that the Ni_xB NPs are still firmly entrapped on the surface of the $YSe_2/MoSe_2$ films, and the films also retain their unique morphology like hybrids. Therefore, the improved electrochemical energy storage of the $YSe_2/MoSe_2/Ni_xB$ electrode could be mainly attributed to the ion buffer reservoirs of $YSe_2/MoSe_2$, which facilitated the fast and continuous charge/discharge process, followed by the improvement of structural integrity with amorphous Ni_xB nanoparticles, obviously leading to good cyclic performance and better rate capability in $YSe_2/MoSe_2/Ni_xB$ electrodes based on SCs. According to FE-SEM, XRD analysis was also performed after the cyclic stability test. The resulting XRD pattern after the 5000-cycle test is shown in Fig. S8. The presence of identical XRD peaks for $YSe_2/MoSe_2/Ni_xB$ with no change in valence was observed. Moreover, there is no obvious change in phase or crystal structure. This XRD result also shows that the $YSe_2/MoSe_2/Ni_xB$ electrode is more stable under alkaline environmental conditions, even with repeated cyclic tests. The overall result of CV, GCD, and EIS analysis shows that the proposed $YSe_2/MoSe_2/Ni_xB$ electrode is perfectly suitable for the fabrication of ASC devices under aqueous electrolyte conditions.

Given the encouraging results obtained with the $YSe_2/MoSe_2/Ni_xB$ hybrid, an asymmetric device was constructed using the hybrid as the positive electrode and rGO as the negative electrode to get a $YSe_2/MoSe_2/Ni_xB||rGO$ device with two electrodes. An aqueous 3 M KOH solution was used as the electrolyte, and paper was kept as the separator. Using charge balance theory, the mass loading of the positive and negative electrodes on the NF substrate was calculated as 2.7 mg. Fig. S9 demonstrates the corresponding CV of $YSe_2/MoSe_2/Ni_xB$ and rGO/NF recorded in 3 M KOH electrolyte using a three-electrode cell. First, the $YSe_2/MoSe_2/Ni_xB||rGO$ device was cycled from 0 V to various upper potential limits at 20 mV s^{-1} to establish a suitable working potential window. These data are shown in Fig. 9(a) and clearly demonstrate that the $YSe_2/MoSe_2/Ni_xB||rGO$ device can be cycled to a relatively high potential of 1.6 V without distorting the shape of the CVs or triggering the oxygen evolution reaction (GCD comparison also shown in (Fig. S9). Fig. 9(b) shows the CV of the device in a potential region of 0–1.6 V at

Table 1

Summary of some previously reported materials used to form supercapacitors, with measured power and energy densities.

Electrode	Substrate	Electrolyte	Operating Voltage/ (V)	Power Density/ (W kg^{-1})	Energy Density/ (Wh kg^{-1})	Ref
Ni$_3$Al||AC-MWCNT	Al foil	1 M Li$_2$SO$_4$	1.5	5	5.9	[41]
RuO$_2$/ECG cells	Ti	0.5 M H$_2$SO$_4$	1	10	9.2	[42]
Zn–Ni–Co-S||gC$_3$N$_4$/rGO	NF	2 M KOH	1.6	419	88	[43]
Bi$_3$YO$_6$||rGO	NF	3 M Na$_2$SO$_4$	2.2	648	11	[44]
MnF$_2$||AC	Carbon felt	3 M KOH	1.8	823	36	[45]
Fe-Co-P@Ni(OH)$_2$||carbon nanofiber	NF	2 M KOH	1.6	536	65	[46]
MnO$_2$/Ni–Mn–S||N-rGO	NF	PVA-KOH	1.8	937	31	[47]
MXene(TiV)$_3$C$_2$T$_x$ (Symmetric)	MXene film	3 M H2SO$_4$	0.7	5210	5.6	[48]
CoB-V-MXene||AC	NF	0.5 M K$_2$SO$_4$	1.6	800	31	[49]
Ni$_x$B/MnMoO$_4$||AC	NF	3 M KOH	1.55	750	32	[23]
1T-MoS$_2$||ZnO/ZnS-C	NF	1 M KOH	1.4	700	66	[50]
MnCo$_2$O$_4$@MoS$_2$||AC	Graphite	6 M KOH-gel	1.9	19	36	[51]
MoS$_2$/BP||Cu foil	NF	PVA-Na$_2$SO$_4$	1.5	4031	34	[52]
YSe$_2$/MoSe$_2$/Ni$_x$B||rGO	NF	3 M KOH	1.6	800	39.5	*This work*

different applied sweep rates. The obtained CV curves are due to the combination of an electrical double-layer capacitance and battery-like behavior. Moreover, the ASC device maintained the same symmetry of the CV traces at higher scan rates, suggesting high capability rate and electron transfer rates. The GCD curves recorded at different current densities from 1 to 20 A/g are shown in Fig. 9(c). A small voltage drop can be seen at the beginning of the discharge curve, which can be attributed to the electrolyte solution resistance and/or the struggle to access the porous network of the YSe$_2$/MoSe$_2$/Ni$_x$B\|\|rGO device. Nevertheless, symmetrical curves with similar charge and discharge times are observed, indicating excellent reversibility. The specific capacitance was calculated as 111.34 F/g (178.15 C/g), 103.25 F/g (82.6 C/g), 96.94 F/g (51.7 C/g), 91.25 F/g (36.5 C/g), 85.63 F/g (27.4 C/g), 63.75 F/g (10.2 C/g), 49.69 F/g (5.3 C/g), and 37.50 F/g (3 C/g) at current densities of 1, 2, 3, 4, 5, 10, 15, and 20 A/g, respectively. Fig. 9(d) shows the Coulombic efficiency and capacitance retention curves recorded at a current density of 10 A/g. The outstanding Coulombic efficiency of 100% is achieved over 5000 charge and discharge cycles, indicating the excellent reversibility of the proposed electrode. Moreover, good cyclic stability is shown with a capacitance retention of 85.60% after 5000 cycles, indicating the strong integrity and mixed heterointerface of YSe$_2$/MoSe$_2$ and Ni$_x$B, which could facilitate the wettability of the electrode in strong alkaline electrolytes. At the same time, the superior cyclic stability of the YSe$_2$/MoSe$_2$/Ni$_x$B\|\|rGO device is due to the following aspects: (i) The presence of numerous active sites and the increase of the surface area of the YSe$_2$ thin sheet and MoSe$_2$ micro flower enables the rapid diffusion of ions over shorter paths and provide more space for volume adjustment during continuous charge/discharge cycles. (ii) In this exclusive hetero nanostructure, the YSe$_2$/MoSe$_2$ base acts as a conducting system for fast electron transfer, and the Ni$_x$B particles act as additional active sites that can establish close contact between the three different components and compensate for the drawbacks of the single structure, resulting in improved mechanical integrity and structural stability. (iii) and integrating the YSe$_2$/MoSe$_2$/Ni$_x$B heterostructure on a conductive NF substrate can prevent the aggregation of the material and improve its mechanical strength. From these aspects, it can be concluded that the YSe$_2$/MoSe$_2$/Ni$_x$B\|\|rGO device exhibits higher Coulombic efficiency and exceptional cyclic stability.

To gain further insight into the stability of the YSe$_2$/MoSe$_2$/Ni$_x$B\|\|rGO device, electrochemical impedance studies were performed before and after 5000 charge and discharge cycles. Representative Nyquist plots are shown in Fig. 9(e). As can be seen from the inset, the x-axis intercept of the Z' axis, which corresponds to the contact and electrolyte resistance, remains essentially constant with a value of 1.56 Ω before and 1.4 Ω after 5000 cycles. The charge transfer resistance also changes only slightly, varying between 0.37 Ω before and 0.46 Ω after the cycles. This low resistance indicates that the fabricated device exhibits efficient charge transfer kinetics maintained after 5000 repeated charge and discharge cycles. In the near linear diffusion region, there is a larger change at the lower frequencies during the continuous cycles. This indicates small fluctuations related to the diffusion of the electrolytic OH$^-$ ions at the electrode interface. Finally, the performance of the YSe$_2$/MoSe$_2$/Ni$_x$B\|\|rGO device is summarized in the Ragone diagram shown in Fig. 9(f), where the power density is plotted as a function of the energy density. Energy and power density were determined using Eqs. (6) and (7), where C_s is the gravimetric specific capacitance, V is the potential window, and Δt is the discharge duration.

$$\text{Energy Density} = 1/2\, C_s V^2 \qquad (6)$$

$$\text{Power Density} = E/\Delta t \qquad (7)$$

As the energy density increases, the power density decreases significantly, which is typical for supercapacitors. At a power density of 800 W kg^{-1}, the energy density reaches an impressive value of 39.5 Wh kg^{-1}, while at a higher power density of 16,000 W kg^{-1}, a somewhat lower energy density of 13.3 Wh kg^{-1} is recorded. These data compare very well with some recently reported supercapacitors, as shown in Table 1. In this table, data from several recently published reports on various metal oxides, MXenes, Ni$_x$B, and MoSe$_2$-based supercapacitors are compared with the YSe$_2$/MoSe$_2$/Ni$_x$B\|\|rGO device fabricated in this work. It is clear that the YSe$_2$/MoSe$_2$/Ni$_x$B\|\|rGO device performs well, outperforms many of the metal boride and MXene-based capacitors, and matches well with the MoSe$_2$-based devices. These results demonstrate that the YSe$_2$/MoSe$_2$/Ni$_x$B\|\|rGO electrode has significant performance for the development of next-generation energy storage systems.

5. Conclusion

In summary, we report a novel ternary YSe$_2$/MoSe$_2$/Ni$_x$B heterostructure based on an asymmetric supercapacitor electrode prepared by facile preparation methods, including hydrothermal and liquid phase routes. The material characterization results show that the strong synergistic effect between YSe$_2$/MoSe$_2$ and Ni$_x$B significantly improves the electrical conductivity and electrochemical performance due to the increased number of active sites after forming the interfaces of crystalline YSe$_2$/MoSe$_2$ and amorphous Ni$_x$B. Due to its superior electrochemical performance, a novel YSe$_2$/MoSe$_2$/Ni$_x$B\|\|rGO-ASC device with a maximum functional potential of 1.6 V was developed, and a higher energy density of 39.5 Wh kg^{-1} was achieved with a power density of 800 W kg^{-1}. In addition, the ASC device demonstrated excellent cycling durability over 5000 cycles with retention of capacitance of 85.60%. These results indicate that they are favorable electrode materials for high-performance energy storage devices. Moreover, the proposed work demonstrates a new route to selecting active transition metal-based heterostructures that can be combined with affordable carbon materials to form novel and promising ASC devices.

CRediT authorship contribution statement

Ramaraj Sukanya: Conceptualization, Methodology, Investigation, Validation, Data curation, Formal analysis, Writing – original draft. **Raj Karthik:** Conceptualization, Methodology, Data curation, Formal analysis, Writing – original draft. **Mahmudul Hasan:** Data curation, Formal analysis, Investigation, Methodology, Writing – review & editing. **Carmel Breslin:** Data curation, Formal analysis, Funding acquisition, Investigation, Supervision, Writing – original draft. **Jae-Jin Shim:** Funding acquisition, Project administration, Supervision, Investigation, Validation, Writing – review & editing.

Declaration of Competing Interest

The authors declare that they have no known competing financial interests or personal relationships that could have appeared to influence the work reported in this paper.

Data availability

Data will be made available on request.

Appendix A. Supplementary data

Supplementary data to this article can be found online at https://doi.org/10.1016/j.cej.2023.145487.

References

[1] X. Chen, J. Zhu, J. Cai, Y. Zhang, X. Wang, Nanosheets assembled layered MXene/MoSe$_2$ nanohybrid positive electrode materials for high-performance asymmetric supercapacitors, J. Energy Storage. 40 (2021), 102721.

[2] S. Singal, A. Yadav, G. Singh, R.K. Sharma, Molybdenum-vanadium diboride core@amorphous nanoporous carbon shell composite as a novel electrode material for hybrid supercapacitor, J. Energy Storage. 54 (2022), 105380.

[3] H. Peng, J. Zhou, K. Sun, G. Ma, Z. Zhang, E. Feng, Z. Lei, High-performance asymmetric supercapacitor designed with a Novel NiSe@MoSe$_2$ nanosheet array and nitrogen-doped carbon nanosheet, ACS Sustain. Chem. Eng. 5 (7) (2017) 5951–5963.

[4] M. Manuraj, S. Jyothilakshmi, K.N. Narayanan Unni, R.B. Rakhi, MoSe$_2$ nanoflowers as efficient electrode materials for supercapacitors, J. Mater. Sci. Mater. Electron. 31 (22) (2020) 20571–20577.

[5] S.K. Balasingam, J.S. Lee, Y. Jun, Few-layered MoSe$_2$ nanosheets as an advanced electrode material for supercapacitors, Dalton Trans. 44 (35) (2015) 15491–15498.

[6] P. Pazhamalai, K. Krishnamoorthy, S. Sahoo, S.J. Kim, Two-dimensional molybdenum diselenide nanosheets as a novel electrode material for symmetric supercapacitors using organic electrolyte, Electrochim. Acta 295 (2019) 591–598.

[7] Rahul, S.K. Arora, Arora MoSe$_2$ nanosheets as an efficient electrode material for supercapacitors, Mater. Today:. Proc. 54 (2022) 728–732.

[8] Y. Liu, W. Li, X. Chang, H. Chen, X. Zheng, J. Bai, Z. Ren, MoSe$_2$ nanoflakes-decorated vertically aligned carbon nanotube film on nickel foam as a binder-free supercapacitor electrode with high-rate capability, J. Colloid Interface Sci. 562 (2020) 483–492.

[9] Q. Shen, P. Jiang, H. He, C. Chen, Y. Liu, M. Zhang, Encapsulation of MoSe$_2$ in carbon fibers as anodes for potassium ion batteries and nonaqueous battery-supercapacitor hybrid devices, Nanoscale 11 (2019) 13511–13520.

[10] S. Ramaraj, M. Sakthivel, S.-M. Chen, K.-C. Ho, Active-site-rich 1T-phase CoMoSe$_2$ integrated graphene oxide nanocomposite as an efficient electrocatalyst for electrochemical sensor and energy storage applications, Anal. Chem. 91 (13) (2019) 8358–8365.

[11] M. Sakthivel, S. Ramaraj, S.-M. Chen, T.-W. Chen, K.-C. Ho, Transition-metal-doped molybdenum diselenides with defects and abundant active sites for efficient performances of enzymatic biofuel cell and supercapacitor applications, ACS Appl. Mater. Interfaces 11 (20) (2019) 18483–18493.

[12] M.S. Vidhya, R. Yuvakkumar, G. Ravi, B. Saravanakumar, D. Velauthapillai, Asymmetric polyhedron structured NiSe$_2$@MoSe$_2$ device for use as a supercapacitor, Nanoscale Adv. 3 (14) (2021) 4207–4215.

[13] J. Yang, C. Wang, H. Ju, Y. Sun, S. Xing, J. Zhu, Q. Yang, Integrated quasiplane heteronanostructures of MoSe$_2$/Bi$_2$Se$_3$ hexagonal nanosheets: Synergetic electrocatalytic water splitting and enhanced supercapacitor performance, Adv. Funct. Mater. 27 (2017), 1703864.

[14] V.S. Kumbhar, A.C. Lokhande, N.R. Chodankar, N.S. Gaikwad, C.D. Lokhande, Self-assembled samarium selenide nanorods as a new electrode material for reliable supercapacitors, Mater. Lett. 223 (2018) 45–48.

[15] B. Pandit, A. Agarwal, P. Patel, B.R. Sankapal, The electrochemical kinetics of cerium selenide nano-pebbles: The design of a device-grade symmetric configured wide-potential flexible solid-state supercapacitor, Nanoscale Adv. 3 (2021) 1057–1066.

[16] S.J. Patil, V.C. Lokhande, N.R. Chodankar, C.D. Lokhande, Chemically prepared La$_2$Se$_3$ nanocubes thin film for supercapacitor application, J. Colloid Interface Sci.. 469 (2016) 318–324.

[17] K. Shree, S. Parveen, S.K. Sharma, S.N. Pandey, Solid-state symmetric supercapacitor based on Y doped Sr(OH)2 using SILAR method, Energy 197 (2020), 117163.

[18] S. Saha, M. Jana, P. Khanra, P. Samanta, H. Koo, N. Chandra Murmu, T. Kuila, Band gap modified boron doped NiO/Fe$_3$O$_4$ nanostructure as the positive electrode for high energy asymmetric supercapacitors, RSC Adv. 6 (2) (2016) 1380–1387.

[19] Y. Zhang, Y. Zhai, Preparation of Y-doped ZrO$_2$ coatings on MnO$_2$ electrodes and their effect on electrochemical performance for MnO$_2$ electrochemical supercapacitors, RSC Adv. 6 (3) (2016) 1750–1759.

[20] S. Carenco, D. Portehault, C. Boissiere, N. Mezailles, C. Sanchez, Nanoscaled metal borides and phosphides: Recent developments and perspectives, Chem. Rev. 113 (2013) 7981–8065.

[21] Y. Zhang, C. Fu, J. Fan, H. Lv, W. Hao, Preparation of Ti@NiB electrode via electroless plating toward high-efficient alkaline simulated seawater splitting, J. Electroanal. Chem. 901 (2021), 115761.

[22] X. Cao, X. Wang, L. Cui, D. Jiang, Y. Zheng, J. Liu, Strongly coupled nickel boride/graphene hybrid as a novel electrode material for supercapacitors, Chem. Eng. J. 327 (2017) 1085–1092.

[23] R. Karthik, R. Sukanya, S.M. Chen, M. Hasan, G. Dhakal, P.M. Shafi, J.-J. Shim, Development of an amorphous nickel boride/manganese molybdate heterostructure as an efficient electrode material for a high-performance asymmetric supercapacitor, ACS Appl. Mater. Interfaces 15 (9) (2023) 11927–11939.

[24] Z. Tian, K. Zhou, M. Xie, Y. Zhang, J. Chen, C. Du, L. Wan, Self-supported nickel iron selenide@nickel cobalt boride core-shell nanosheets electrode for asymmetric supercapacitors, Chem. Eng. J. 447 (2022), 137495.

[25] M. Sakthivel, R. Sukanya, S.-M. Chen, K.-C. Ho, Synthesis and characterization of samarium-substituted molybdenum diselenide and its graphene oxide nanohybrid for enhancing the selective sensing of chloramphenicol in a milk sample, ACS Appl. Mater. Interfaces 10 (35) (2018) 29712–29723.

[26] N.V. Podberezskaya, V.Y. Komarov, R.E. Nikolaev, T.P. Chusova, L.N. Zelenina, B.M. Kuchumov, I.V. Korol'kov, Tetragonal stoichiometric yttrium diselenide, J. Struct. Chem.. 60 (1) (2019) 92–98.

[27] P. Malacrida, H.G. Sanchez Casalongue, F. Masini, S. Kaya, P. Hernández-Fernández, D. Deiana, H. Ogasawara, I.E.L. Stephens, A. Nilsson, I.b. Chorkendorff, Direct observation of the dealloying process of a platinum-yttrium nanoparticle fuel cell cathode and its oxygenated species during the oxygen reduction reaction, PCCP 17 (42) (2015) 28121–28128.

[28] A.E. Elkholy, F.E.T. Heakal, N.K. Allam, A facile electrosynthesis approach of amorphous Mn-Co-Fe ternary hydroxides as binder-free active electrode materials for high-performance supercapacitors, Electrochim. Acta 296 (2019) 59–68.

[29] S.X. Yan, S.H. Luo, J. Feng, P.W. Li, R. Guo, Q. Wang, Y.H. Zhang, Y.G. Liu, S. Bao, Rational design of flower-like FeCo$_2$S$_4$/reduced graphene oxide films: Novel binder-free electrodes with ultra-high conductivity flexible substrate for high-performance all-solid-state pseudocapacitor, Chem. Eng. J. 381 (2020), 122695.

[30] S.X. Yan, Q. Wang, S.H. Luo, Y.H. Zhang, X. Liu, Y.G. Liu, Z. Wang, A. Hao, T.F. Yi, Coal-based S hybrid self-doped porous carbon for high-performance supercapacitors and potassium-ion batteries, J. Power Sources 461 (2020), 228151.

[31] S.X. Yan, S.H. Luo, M.Z. Sun, Q. Wang, Y.H. Zhang, X. Liu, Facile hydrothermal synthesis of urchin-like NiCo$_2$O$_4$ as advanced electrochemical pseudocapacitor materials, Int. J. Energy Res. 1–13 (2021).

[32] Y. Gao, K. Liu, Y. Wu, C. Li, Q. Lu, G. Zu, A strategy of combination reaction to improve electrochemical performance in two-dimensional Mo$_{1-x}$W$_x$Se$_2$ battery-type electrode materials, Ceram. Int. 49 (2023) 7196–7207.

[33] J. Masa, I. Sines, H. Mistry, E. Ventosa, M. de la Mata, J. Arbiol, M. Muhler, B. Roldan Cuenya, W. Schuhmann, Ultrathin high surface area nickel boride (NixB) nanosheets as highly efficient electrocatalyst for oxygen evolution, Adv. Energy Mater. 7 (2017) 1700381.

[34] M. Sathiya, A.S. Prakash, K. Ramesha, J—M. Tarascon, A.K. Shukla, V$_2$O$_5$ anchored carbon nanotubes for enhanced electrochemical energy storage, J. Am. Chem. Soc. 133 (40) (2011) 16291–16299.

[35] L. Ma, L. Xu, X. Zhou, X. Xu, L. Zhang, Synthesis of a hierarchical MoSe$_2$/C hybrid with enhanced electrochemical performance for supercapacitors, RSC Adv. 6 (94) (2016) 91621–91628.

[36] M.S. Vidhya, R. Yuvakkumar, P.S. Kumar, G. Ravi, D. Velauthapillai, Hydrothermal synthesis of flower like MnSe$_2$@MoSe$_2$ electrode for supercapacitor applications, Top. Catal. 65 (2022) 615–622.

[37] S.K. Balasingam, J.S. Lee, Y. Jun, Molybdenum diselenide/reduced graphene oxide-based hybrid nanosheets for supercapacitor applications, Dalton Trans. 45 (23) (2016) 9646–9653.

[38] S.-X. Yan, S.-H. Luo, J. Feng, L. Yang, P.-W. Li, Q. Wang, Y.-H. Zhang, X. Liu, L.-J. Chang, Asymmetric, flexible supercapacitor based on Fe-Co Alloy@Sulfide with high energy and power density, ACS Appl. Mater. Interfaces 13 (42) (2021) 49952–49963.

[39] S.X. Yan, S.H. Luo, Q. Wang, Y.H. Zhang, X. Liu, Rational design of hierarchically sulfide and MXene-reinforced porous carbon nanofibers as advanced electrode for high energy density flexible supercapacitors, Compos. B Eng. 224 (2021) 109246.

[40] S.X. Yan, S.H. Luo, H. Liu, L. Yang, Q. Wang, Y.H. Zhang, X. Liu, In-situ partial reduction–sulfurized Fe$_3$O$_4$@FeS based on pickling iron red as a versatile electrode for high-performance lithium-ion batteries and supercapacitor devices, Surf. Coat. Tech. 429 (2022), 127980.

[41] R. Vicentini, W.G. Nunes, L.H. da Costa, L.M. Da Silva, B. Freitas, A.M. Pascon, O. Vilas-Boas, H. Zanin, Multi-walled carbon nanotubes and activated carbon composite material as electrodes for electrochemical capacitors, J. Energy Storage. 33 (2021), 100738.

[42] J.D. Xie, J. Patra, A.T.I. Muhammad, Y.A. Gandomi, T.Y. Wu, S.W. Lee, J.K. Chang, Graphene induced crystallinity and hydrous state variations of ruthenium oxide electrodes for superior energy storage performance, Electrochim. Acta 360 (2020), 136995.

[43] P. Bandyopadhyay, G. Saeed, N.H. Kim, S.M. Jeong, J.H. Lee, Fabrication of hierarchical Zn-NiCoS nanowire arrays and graphitic carbon nitride/graphene for solid-state asymmetric supercapacitors, Appl. Surf. Sci. 542 (2021), 148564.

[44] M. Sajjad, S.U. Asif, L. Guan, Y. Jiao, Y. Jiang, L. Zhang, J. Wen, S. Zhang, Y. Lin, S. Zhang, Z. Ding, Y. Ren, X. Zhou, W. Hu, Z. Liu, Bismuth yttrium oxide (Bi3YO6), a new electrode material for asymmetric aqueous supercapacitors, J. Inorg. Organomet. Polym Mater. 31 (3) (2021) 1260–1270.

[45] P. Sivaprakash, K.A. Kumar, K. Subalakshmi, C. Bathula, S. Sandhu, S. Arumugam, Fabrication of high-performance asymmetric supercapacitors with high energy and power density based on binary metal fluoride, Mater. Lett. 275 (2020), 128146.

[46] J. Chen, P. Bandyopadhyay, E.M. Jin, S.M. Jeong, Rationally designed hierarchical tree-like Fe-Co-P@Ni(OH)2 hybrid nanoarrays for high energy density asymmetric supercapacitors, Appl. Surf. Sci. 588 (2022), 152857.

[47] Y.K. Sonia, S.K. Meher, Hierarchical MnO$_2$/NiS-MnS with rich electro-microstructural physiognomies for highly efficient all-solid-state hybrid supercapacitors, Energy Fuels 37 (5) (2023) 4010–4025.

[48] J. Xiao, P. Yu, K. Zhao, H. Gao, Two-dimensional transition metal carbide (Ti0.5V0.5)3C2Tx MXene as high-performance electrode for flexible supercapacitor, J. Colloid Interface Sci. 639 (2023) 233–240.

[49] R. Venkatkarthick, J. Qin, T. Maiyalagan, Amorphous cobalt boride nanoparticles incorporated vanadium carbide MXene composite for asymmetric supercapacitor applications, Int. J. Energy Res. 46 (15) (2022) 22474–22485.

[50] Z. Wang, J. Wang, F. Wang, X. Zhang, X. He, S. Liu, Z. Zhang, Z. Zhang, X. Wang, One-step hydrothermal synthesis of high-performance stable Ni-doped 1T-MoS$_2$ electrodes for supercapacitors, J. Alloy. Compd. 947 (2023), 169505.

[51] P.S. Shukla, A. Agrawal, A. Gaur, G.D. Varma, Facile synthesis of mesoporous MnCo$_2$O$_4$@MoS$_2$ nanocomposites for asymmetric supercapacitor application with excellent prolonged cycling stability, J. Energy Storage. 59 (2023), 106580.

[52] S. Radhakrishnan, N. Kuniyil, A. Sharma, C.S. Rout, Hierarchal growth of integrated n-MoS$_2$/p-black phosphorus heterostructures for all-solid-state asymmetric supercapacitor electrodes, Energy Fuels 37 (4) (2023) 3196–3207.